$YVO_4:Er^{3+}/Yb^{3+}$ phosphor for multifunctional applications

Manoj Kumar Mahata,[1,2] Surya Prakash Tiwari,[1] Shriparna Mukherjee,[1] Kaushal Kumar,[1,*] and Vineet Kumar Rai[1]

[1]*Department of Applied Physics, Indian School of Mines, Dhanbad 826004, India*
[2]*II-Physikalisches Institut, Georg-August-Universität Göttingen, Friedrich-Hund-Platz 1, 37077 Göttingen, Germany*
**Corresponding author: kumar.bhu@gmail.com*

Received March 18, 2014; accepted April 19, 2014;
posted June 2, 2014 (Doc. ID 208360); published July 10, 2014

This article reports luminescence studies on wet-chemical route prepared $YVO_4:Er^{3+}/Yb^{3+}$ microdisc phosphor. The 980 nm laser excited upconversion (UC) emission intensity ratio of green to red bands is found too high to neglect the contribution from the red emission band, which is not observed normally in Er^{3+}/Yb^{3+}-doped materials. The red emission is also found absent in the downconversion emission under excitation at 316 nm. The variation of UC intensities with external temperature exhibits a well-fashioned pattern, which suggests that the $^2H_{11/2}$ and $^4S_{3/2}$ levels of Er^{3+} ion are thermally coupled. The $YVO_4:Er^{3+}/Yb^{3+}$ phosphor has shown outstanding temperature-sensing behavior with maximum sensitivity of 0.0117 K^{-1} at 400 K. This material is also employed to develop a latent fingerprint in green color. Furthermore, the present phosphor could be useful for solar cell concentrators, drug delivery, and disease therapy applications.

OCIS codes: (300.0300) Spectroscopy; (160.4760) Optical properties.
http://dx.doi.org/10.1364/JOSAB.31.001814

1. INTRODUCTION

Rare earth ion-doped conventional materials are now under reinvestigation in the light of nanotechnology since nanomaterials have shown improved and novel optical properties [1–3]. The research is progressing in this direction because these materials have outstanding applications as optical sensors, optical amplifiers, multicolor displays and lighting devices, luminescent concentrators in solar panels, lasers [1–5], etc. Moreover, photon upconverting materials offer advantages for biological applications because of low autofluorescence from surrounding tissues, high spatial resolution, and high penetration depth of excitation wavelength [6–10].

Yttrium orthovanadate has excellent physical and optical properties [11] and is highly birefringent. It is used in various optical devices, including Nd:YVO_4 laser [12]. For an efficient NIR to visible upconversion, the host should have low phonon energy. YVO_4 lattice has phonon energy of 880 cm^{-1} and exhibits good upconversion efficiency when it is doped with RE ions [11,13]. It also has a zircon-type structure, described by the general formula $A^{+m}B^{+(8-n)}O_4$, where A, B are metal ions having a coordination number of 8 and 4, respectively [14]. The zircon-type YVO_4 is built from the chains of alternating edge-sharing VO_4 and YO_8. The tetragonal YVO_4 crystal belongs to the D_{4h} space group, with D_{2d} the local point symmetry of Y^{3+}, and is surrounded by eight O^{2-} ions at the vertices of a tetragonal dodecahedron. The ionic radii of Er^{3+} (0.881 Å) and Yb^{3+} (0.858 Å) are close to that of Y^{3+} (0.90 Å). So the yttrium ion in the D_{2d} site of the YVO_4 lattice is easily substituted by erbium and ytterbium ions [15].

It is known that under UV excitation, the energy transfer from the excited YVO_4 host to the trivalent RE ions takes place, and this process is effective in overcoming low absorption of RE ions. In this case, VO_4^{3-} groups are excited from the ground state, and, when the energy-matching condition is fulfilled, these excited ions serve as a universal sensitizer for RE ions [16]. Er^{3+} is an active dopant for downconversion as well as IR to visible upconversion emission because of its favorable electronic energy levels with long-lived excited states. Yb^{3+} ions, with one excited energy state ($^2F_{5/2}$), have a large absorption cross section at around 980 nm [17]. The energy difference between ground state ($^2F_{7/2}$) and excited state ($^2F_{5/2}$) of Yb^{3+} ion matches very well with the energy difference between $^4I_{11/2}$ and $^4I_{15/2}$ and $^4I_{11/2}$ and $^4F_{7/2}$ energy states of Er^{3+} ion and thus causes an efficient energy transfer from Yb^{3+} to Er^{3+} ion. Finally, by codoping with Yb^{3+}, the pump efficiency for upconversion gets enhanced.

Downconversion luminescence in $YVO_4:Nd^{3+}$, $YVO_4:Bi^{3+}/Eu^{3+}$, $YVO_4:Ln^{3+}$ (Ln = Eu, Dy, Sm) has been studied in several works [18–22]. Eu^{3+}-doped YVO_4 red phosphors are widely used in cathode ray tube displays. It is also a promising candidate for plasma display panels. Sun *et al.* [23] reported white light generation in an upconversion emission mode from Er^{3+}, Yb^{3+}, Ho^{3+}, and Tm^{3+} ions-codoped YVO_4. The upconversion luminescence in Er^{3+}/Yb^{3+}-codoped YVO_4 phosphors also has been studied by several other researchers [24,25].

Accurate sensing and mapping of temperature in a noninvasive way is a challenging field of research because of the use of thermal sensors in micro- and nanoscale electronic and photonic devices [26]. Recently the optical temperature sensors based on monitoring the temperature by using the fluorescence intensity ratio (FIR) technique, which play a vital role in the places where conventional sensors (so-called contact thermometers) cannot be used. For an efficient optical temperature sensor, the sensitivity should be high. Therefore the search for this kind of material is challenging.

In this work, we have prepared the Er^{3+}/Yb^{3+}-doped YVO_4 phosphor using a simple wet-chemical coprecipitation method and studied the emission properties using 316 and 980 nm excitations. High purity green emission is observed in the prepared sample. The sample is optically investigated for various optical applications.

2. EXPERIMENTS

A. Synthesis of YVO_4:Er^{3+}/Yb^{3+} Microdiscs

The crystalline YVO_4 powder was synthesized with 3 mol% Yb^{3+} and 0.3 mol% Er^{3+} doping concentrations via a wet-chemical route. The starting materials viz. V_2O_5 (Sigma Aldrich), Y_2O_3 (Merck), Er_2O_3 (Merck), and Yb_2O_3 (Merck) were purchased with 99.99% purity. The oxides were taken as stoichiometric proportion, and their nitrate forms were prepared by dissolving these oxides in concentrated nitric acid. All these nitrates were mixed in a beaker with double distilled water in order to remove the excess acid and then placed on a magnetic stirrer whose hotplate was maintained at 80°C for 3 h. Citric acid was added as a chelating agent for metal ions, keeping the molar ratio of metal ions to citric acid at 1:2. The chelating agent prevents the agglomeration of particles at reaction time and thus leads to form smaller particles. After that, ammonium hydroxide (NH_4OH) was mixed drop-wise under vigorous stirring. The pH of the resulting solution was kept at 8.0. The solution of these reagents was stirred on a magnetic stirrer maintained at 80°C followed by 1 h ultrasonic agitation for uniform mixing. After 36 h, the resulting precipitate was separated by centrifugation, washed with distilled water and ethanol several times, and dried at room temperature. The as-obtained powder was heated at 800°C for 2 h in order to remove organic impurities.

B. Characterization of Microdiscs

The crystal structure of the sample was determined from an x-ray diffraction pattern taken on a Bruker D8 advanced x-ray diffractometer. The pattern was recorded over the angular range $10° \le 2\theta \le 90°$ using Cu-kα (1.5405 Å) radiation with a scanning rate of 4 deg per min. An infrared absorption spectrum was recorded on a FTIR spectrometer (Perkin Elmer, Spectrum RX I) with 1 cm^{-1} resolution using a KBr pellet technique in the wavenumber range of 4000 to 400 cm^{-1}. Surface morphology was studied from SEM images taken by a JSEM 6390LV (Jeol, Japan). The UV–visible–NIR absorption spectrum was taken in diffuse reflectance mode on a Lambda 950, UV-VIS-NIR spectrophotometer (Perkin Elmer). Downconversion photoluminescence studies were carried out on a Hitachi fluorescence spectrometer, model F-2500. Upconversion emission spectra were recorded on a SP2300 grating spectrograph (Princeton Instruments, USA) using a 980 nm cw diode laser as the excitation source. Resolution of the spectrometer was 0.15 nm with a photomultiplier tube. For temperature-dependent measurements, a pellet of the powder sample was made and placed in a small homemade furnace. The temperature was measured with the help of a thermocouple located closer to the sample as it was heated up.

3. RESULTS AND DISCUSSION

A. Structural Investigations

1. X-ray Diffraction Study

Figure 1(a) shows the x-ray diffraction pattern of YVO_4 powder prepared at 800°C. The pattern was compared with the standard (JCPDS pdf no. 76-1649) file for the tetragonal structure of YVO_4, and corresponding diffraction planes are indexed.

The crystallite size was calculated using the Debye–Scherrer formula and Williamson–Hall equation [27]. The Scherrer formula is given by

$$D = \frac{0.9\lambda}{\beta \cos\theta}, \tag{1}$$

and the Williamson–Hall equation is

$$\frac{\beta \cos\theta}{\lambda} = \frac{1}{D} + \frac{\varepsilon \sin\theta}{\lambda}, \tag{2}$$

where D is the crystallite size, λ is the wavelength of radiation, β is the FWHM of the diffraction peak, θ is the diffraction angle, and ε is the microstrain present in the sample. Microstrain is represented by the slope of the Williamson–Hall plot [Fig. 1(b)].

The average crystallite size calculated using Williamson–Hall plot was 17 nm, while with a Debye–Scherrer formula it was found within the 16–25 nm range. The negative slope

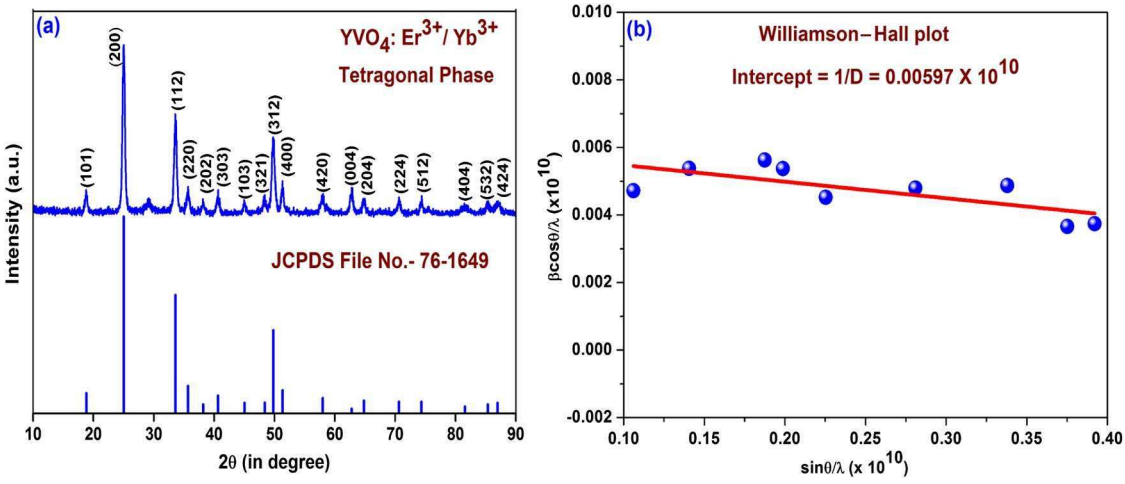

Fig. 1. (a) XRD pattern of the YVO_4:Er^{3+}/Yb^{3+} crystals annealed at 800°C. (b) Williamson–Hall plot of YVO_4:Er^{3+}/Yb^{3+} nanophosphor.

of the W–H plot indicates the contraction of the host lattice due to substitution of Y^{3+} (0.90 Å) ions by slightly lower ionic radii Er^{3+} (0.88 Å) and Yb^{3+} ions (0.86 Å).

The average crystallite size is found around 17 nm, which is lower than the particle size obtained by SEM studies. So it is concluded that a single microdisc particle contains several crystallites.

2. FTIR Analysis

The FTIR spectrum of the heat-treated sample (Fig. 2) shows a low quantity of organic impurities. A broad band around 3400 cm^{-1} is due to the O–H stretching vibrations of H_2O, adsorbed to the surface of the nanocrystals. The band at 2350 cm^{-1} is assigned to the asymmetrical stretching modes of CO_2. This indicates that the annealed sample adsorbs CO_2 from the environment. The weak bands at 1656 and 1628 cm^{-1} correspond to the O–H stretching vibration modes for coordinated water. Another weak band at 1500 and 1408 cm^{-1} may be assigned to the vibration of carboxylate anions in the citric acid. The strong band at 815 cm^{-1} is associated with the characteristic vibrational mode of the V–O bond of VO_4^{3-} groups [28]. The peak at 453 cm^{-1} is due to the characteristic vibrational mode of the Y–O band.

3. SEM Study

Figures 3(a) and 3(b) show the SEM images of the prepared $YVO_4:Er^{3+}/Yb^{3+}$ powder. It shows the disc-shaped particles with a diameter in the range of 200–500 nm. The EDS spectrum [Fig. 3(c)] shows the presence of yttrium, vanadium, and oxygen atoms. It does not show any impurity.

The chemical composition according to EDS analysis is found to be $Y_{0.961}VO_3$. A low weight percentage of oxygen is observed, which may be due to the creation of oxygen deficiency at a high-temperature heat treatment. Low concentrations of Er^{3+} and Yb^{3+} ions are not observed.

B. Optical Studies

1. Diffuse Reflectance Study

The diffuse reflectance spectrum of Er^{3+}/Yb^{3+}-doped YVO_4 powder phosphor was measured against a reference standard

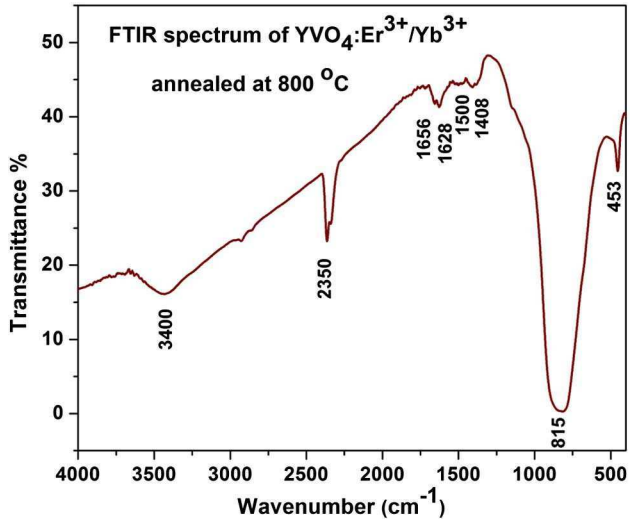

Fig. 2. FTIR spectrum of $YVO_4:Er^{3+}/Yb^{3+}$ phosphor annealed at 800°C.

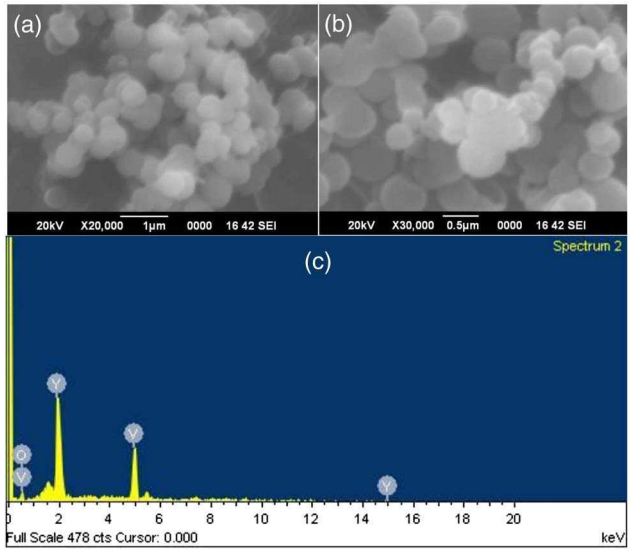

Fig. 3. (a) and (b) SEM images. (c) EDS spectrum of Er^{3+}/Yb^{3+}:YVO_4 nanophosphor.

$BaSO_4$ compound. In diffuse reflectance spectrum, the bands at 490, 522, 654, and 974 nm were observed (Fig. 4). The strong band at around 330 nm is due to the bandgap of the material. The absorption bands at 490, 522, and 654 nm are the transitions from the ground state, $^4I_{15/2}$ to the excited $^4F_{7/2}$, $^2H_{11/2}$, and $^4F_{9/2}$ states of Er^{3+} ion. The broad band around 974 nm is due to the transition from the $^2F_{7/2}$ state to the Stark spilt $^2F_{5/2}$ state of Yb^{3+} ion. The spectrum shows a broad band in the wavelength region 210 to 340 nm. It is attributed to the bandgap of the host matrix.

The bandgap of yttrium vanadate is calculated using the Kubelka–Munk theory [29] from diffuse spectrum and is found to be 3.78 eV. This result matches well with the reported value (3.79 eV) in the literature [30].

2. Downconversion Luminescence Study

Under 316 nm UV excitation, Er^{3+} – Yb^{3+}-doped YVO_4 nanocrystals showed green emission bands at 527 and 555 nm wavelengths [Fig. 5(a)]. This green luminescence is due to the intra-4f transition of the Er^{3+} ion in the D_{2d} site. The VO_4^{3-} groups in the YVO_4 host are excited via absorbing UV photons;

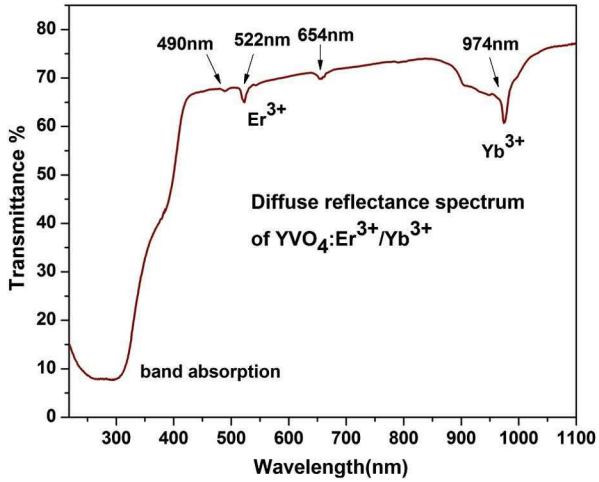

Fig. 4. Diffuse reflectance spectrum of Er^{3+}/Yb^{3+}-doped YVO_4.

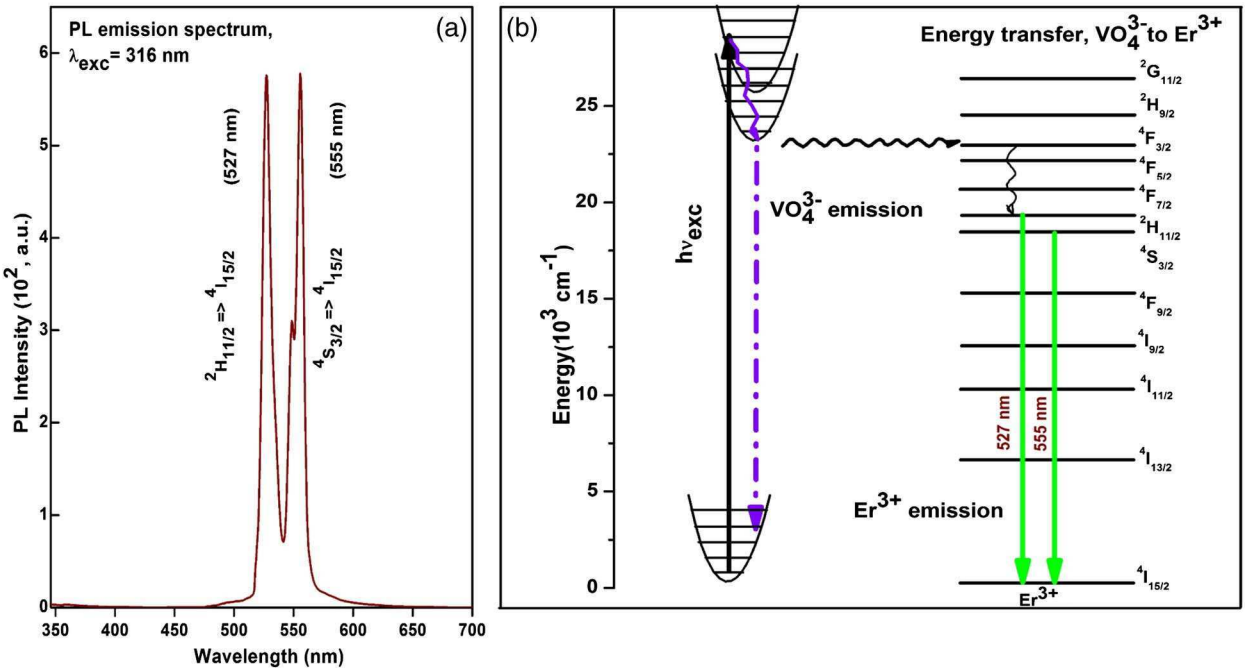

Fig. 5. (a) Luminescence ($\lambda_{exc} = 316$ nm) spectrum of Er^{3+}/Yb^{3+}:YVO_4. (b) Schematic diagram of emission process.

then excited VO_4^{3-} groups serve as a sensitizer for the Er^{3+} activators. As a result of energy transfer from the vanadate group to the Er^{3+} ion, green emission is observed. The energy transfer process is shown in Fig. 5(b). The energy transfer efficiency depends on the angle formed by the central absorption atom, oxygen ion, and erbium ion. From magnetic studies, it is known that the superexchange interaction between paramagnetic ions depends on the angle made by the paramagnetic ion, oxygen ion, and paramagnetic ion. This superexchange interaction is stronger in σ bonding (angle 180°) compared with π bonding (angle 90°). In YVO_4, the V-O-Y angle is of 170°, so it almost overlaps with π bonding, and an efficient energy transfer occurs from VO_4^{3-} to Er^{3+} ions [28]. Interestingly, there is no emission due to the $^4F_{9/2} \rightarrow {}^4I_{15/2}$ transition (red emission). It suggests that there is a negligible nonradiative transition from the $^4S_{3/2}$ level to the $^4F_{9/2}$ level in this phosphor.

3. Upconversion Emission Study

Upconversion emission is studied upon 980 nm excitation. The emission spectrum is shown in Fig. 6. The upconversion luminescence showed strong green emission at 525 and 554 nm and weak red luminescence at 661 nm. The energy level diagram for Er^{3+} and Yb^{3+} ions and various feasible excitation pathways are shown in our previous report [31]. The luminescence bands can be attributed to $^2H_{11/2} \rightarrow {}^4I_{15/2}$ and $^4S_{3/2} \rightarrow {}^4I_{15/2}$ transitions for 525 and 554 nm peaks, respectively, while the $^4F_{9/2} \rightarrow {}^4I_{15/2}$ transition produces red emission of 661 nm. Here, Yb^{3+} acts as a sensitizer. The excitation wavelength (980 nm) is in resonance with the $^2F_{7/2} \rightarrow {}^2F_{5/2}$ transition of the Yb^{3+} ion and thus absorbed by the ion. An efficient energy transfer between Yb^{3+} and Er^{3+} ions occurs due to the spectral overlap between the $^2F_{5/2} \rightarrow {}^2F_{7/2}$ (Yb^{3+}) transition and the $^4I_{11/2} \rightarrow {}^4I_{15/2}$ (Er^{3+}) transition. The peak at 546 nm is a Stark component of the $^4S_{3/2}$ level. Pump radiation induces a transition between the ground state $^4I_{15/2}$ and $^4I_{11/2}$ through the ground state absorption process. Then, in the second excitation, the ion is further excited from $^4I_{11/2}$ to $^4F_{7/2}$. The $^4F_{7/2}$ level decays to $^4S_{3/2}$ and $^2H_{11/2}$ levels nonradiatively. A cooperative energy transfer process between two Er^{3+} ions cannot be ignored here. In this process, two Er^{3+} ions at the $^4I_{11/2}$ level interact each other, and one Er^{3+} ion is de-excited to the ground level, whereas the other one is excited at the $^4F_{7/2}$ level. The red intensity is low in comparison with that of the green. This is due to the fewer number of nonradiative transitions of erbium ions to the $^4F_{9/2}$ level, which makes a low population at this level. The lifetime of the $^2H_{11/2}$ and $^4S_{3/2}$ levels were calculated using a single exponential fitting (inset of Fig. 6) and were found to be 973 and 681 μs, respectively.

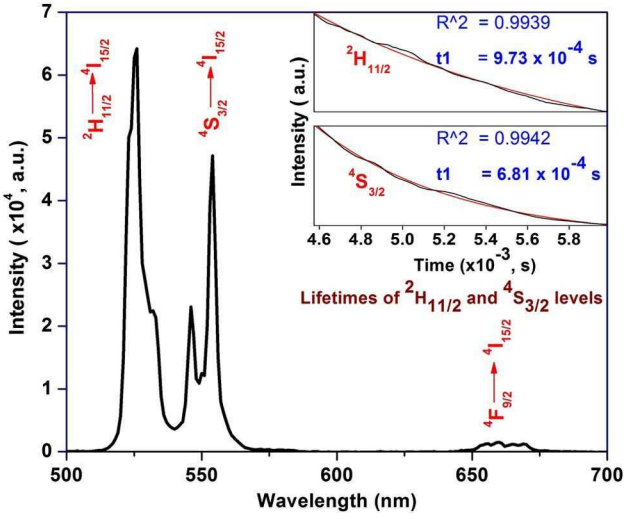

Fig. 6. UC emission spectrum (at power 203 mW) of YVO_4:Yb^{3+}/Er^{3+} nanophosphor (inset shows the lifetime decay curves of $^2H_{11/2}$, and $^4S_{3/2}$ levels with single exponential fitting).

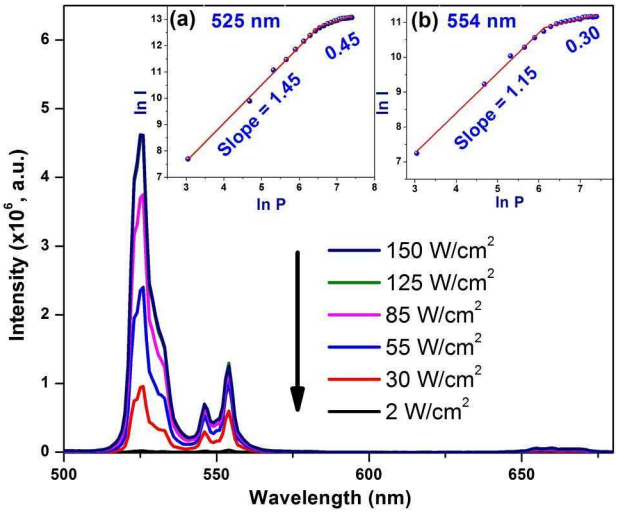

Fig. 7. Variation of UC emission intensity with different excitation powers (inset shows the ln I-ln P plot of 525 and 554 nm emission bands).

4. *Excitation Power Dependence of Upconversion Emission Intensity*

To understand the upconversion mechanisms, the UC emission intensity was measured with input laser excitation power. In the low input power limit, the upconversion emission intensity is related to the power as $I(P) \propto P^n$, where n is the number of IR photons that must be absorbed for the emission of one upconversion photon. So the plot of ln I(P) versus ln P gives the nature of upconversion, i.e., the number of photons absorbed in the upconversion process. Figure 7 shows the power dependence of emission bands located at 525 and 554 nm wavelengths. The slopes of the log-log plot of power and intensity are found to become saturated at higher excitation power (inset of Fig. 7). Power dependence of the two green peaks was analyzed according to the model provided by Suyver *et al.* [32], which shows that the $^2H_{11/2} \rightarrow {}^4I_{15/2}$ (~525 nm) and $^4S_{3/2} \rightarrow {}^4I_{15/2}$ (~554 nm) transitions are two-photon absorption processes. The upconversion efficiency is governed by the nonradiative processes. As the power is increased, heat is generated in the sample. Here, it is to be mentioned that the nonradiative processes depend on the energy gap between the associated higher- and lower-energy transition levels as well as the phonon energy of the material. With increasing temperature, the stimulated emission of phonons by thermal phonons increases, and the multiphonon nonradiative decay rate can be presented according to energy gap law as [33]

$$W_{mp}(T) = W_{mp}(0)\left[1 - e^{-\frac{h\vartheta}{kT}}\right]^{-n}, \tag{3}$$

where $W_{mp}(T)$ and $W_{mp}(0)$ are the nonradiative decay rate at temperature T and 0 K, respectively, $h\nu$ is the relevant phonon energy, $n = \Delta E/h\nu_{max}$ is the minimum number of phonons required to bridge the energy gap ΔE between the relaxing and next lower state, and $h\nu_{max}$ is the highest energy of the phonon. This equation shows that if the phonon energy of the material is low, the nonradiative relaxations are obstructed, and hence the upconversion emission increases. When the energy gap between the two relevant levels becomes equal to three to four times the phonon energy, the multiphonon relaxation process is found to be competitive with the radiative process. The multiphonon decay rate due to spontaneous phonon emission at 0 K from an excited state is given by [34]

$$W_{mp}(0) = \beta e^{-\alpha(\Delta E - 2h\vartheta_{max})}, \tag{4}$$

where α and β are the characteristic positive constants of the host material.

Also the high vibrational frequency modes of the chemical functional groups such as O–H, H–C–H, and C–O (existence proved by FTIR spectrum) increases the nonradiative decays. Therefore, for highly efficient upconversion, the presence of these organic impurities must be removed.

The intensity ratio of the peaks centered at 525 and 554 nm is plotted with the excitation power and is shown in Fig. 8(a). This type of variation may be considered as temperature-dependent behavior, because a similar pattern is obtained in the temperature-dependent study [Fig. 8(b)]. It is observed that, upon increasing the pump power, the intensity ratio first increases in a well fashion and then becomes saturated. This may happen due to the population saturation of the excited energy levels at higher power densities. This type of variation

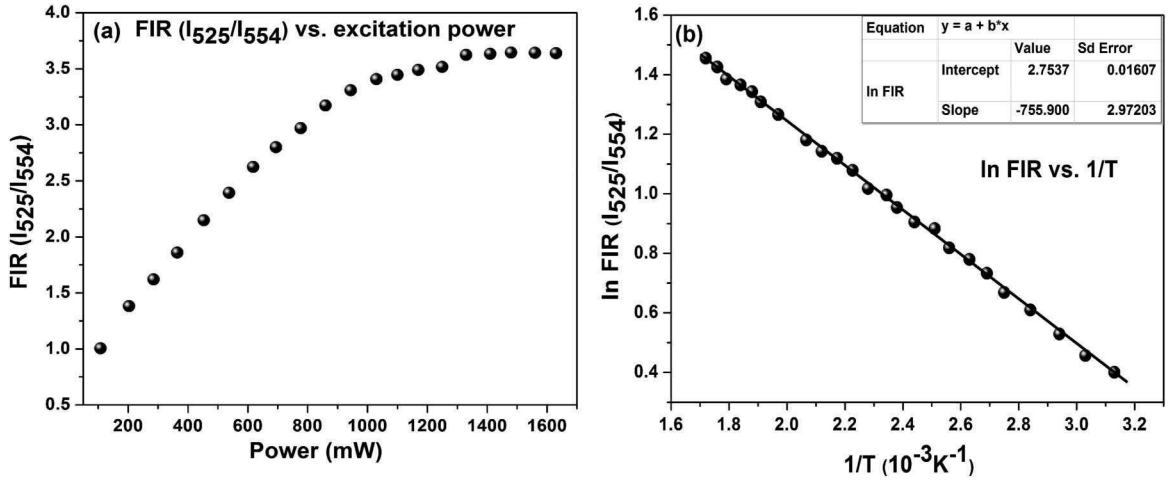

Fig. 8. (a) Fluorescence intensity ratio of $^2H_{11/2} \rightarrow {}^4I_{15/2}$ and $^4S_{3/2} \rightarrow {}^4I_{15/2}$ transitions with pump power. (b) Monolog plot of the FIR (I_{524}/I_{554}) as a function of inverse absolute temperature.

of upconversion emission intensities with excitation power leads us to investigate the frequency upconverted green emissions associated with the two thermally coupled transitions from the $^2H_{11/2}$ and $^4S_{3/2}$ levels to the $^4I_{15/2}$ level of Er^{3+} ion as a function of external temperature.

5. Temperature-Sensing Performance of Er^{3+}/Yb^{3+}-Doped YVO_4 Phosphor

Optical temperature sensors based on the FIR technique [2,31,35,36] have been of considerable interest over the last few years. To study the temperature-sensing performance of the $YVO_4:Er^{3+}/Yb^{3+}$ phosphor, the upconversion emission spectra have been recorded with monitoring the temperature from 302 to 582 K. With an increase in temperature, the band positions do not shift, only the intensity of the green bands changes. The FIR varies with temperature as

$$\mathrm{FIR} = \frac{I_{525}}{I_{554}} = B \exp\left(-\frac{\Delta E}{K_B T}\right), \tag{5}$$

where I_{525} and I_{554} are the integrated intensities corresponding to the $^2H_{11/2} \rightarrow {}^4I_{15/2}$ (~525 nm) and $^4S_{3/2} \rightarrow {}^4I_{15/2}$ (~554 nm) transitions of Er^{3+}, ΔE is the energy gap between the two emitting levels, K_B is the Boltzmann constant, and T is the absolute temperature. Figure 8(b) shows the monolog plot of FIR as a function of the inverse absolute temperature (T), and B is given by the following equation:

$$B = \frac{W_H g_H h\nu_H}{W_S g_S h\nu_S}, \tag{6}$$

where W_H and W_S are the radiative probabilities of two transitions, g_H and g_S are the $(2J + 1)$ degeneracies of levels $^2H_{11/2}$ and $^4S_{3/2}$, respectively, and $h\nu_H$ and $h\nu_S$ are the photon energies of the $^2H_{11/2} \rightarrow {}^4I_{15/2}$ and $^4S_{3/2} \rightarrow {}^4I_{15/2}$ transitions, respectively.

From the least-squares fitting of $\ln(I_{525}/I_{554})$ versus 1/T, the energy gap ΔE and pre-exponential factor B were calculated. The value of the slope, $\Delta E/K_B$, is about 755.9, and from this value ΔE is found as 525 cm^{-1}. The parameter B is found from the y intercept as 15.5, which indicates that the radiative transition probability W_H is much greater than W_S.

It is important to know that the thermal sensitivity of the material is defined as the rate at which the FIR changes with temperature. The sensor sensitivity is defined by

$$S = \frac{\partial(\mathrm{FIR})}{\partial T} = \mathrm{FIR} \times \frac{\Delta E}{K_B T^2}, \tag{7}$$

which is presented in Fig. 9. With the increase in temperature, the sensitivity of the present material decreases. The maximum value is observed as 0.0117 K^{-1} at 400 K, which compares favorably with all other host materials reported in the literature [37]. This achievement suggests that this material could be selected as a potential candidate for a highly sensitive optical temperature sensor based on the FIR technique.

6. $YVO_4:Er^{3+}/Yb^{3+}$ Powder for Latent Fingerprint Detection

Fingerprint detection using upconversion luminescence is advantageous because it gives no background signal [38]. A good affinity for fingerprint ridges on glass by $YVO_4:Er^{3+}/Yb^{3+}$ dry

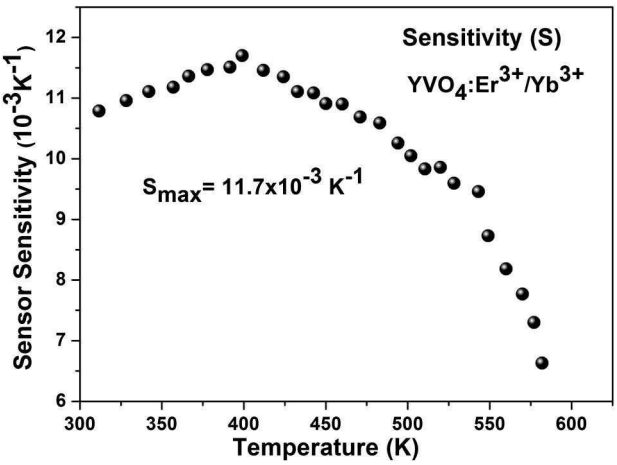

Fig. 9. Sensitivity (S) as a function of absolute temperature (T).

powder was observed. Because of this, the fingerprint on a glass slide was developed using the synthesized powder. Figure 10(a) shows the image of fresh fingerprints developed by dry powdering under 980 nm illumination. The image was photographed by a Nicon D300 camera of 80 mm focal length. The $YVO_4:Er^{3+}/Yb^{3+}$ particles are not the most efficient phosphor, yet it yields satisfactory fingerprint images upon 980 nm diode laser excitation. Therefore the latent fingerprint-detection technique using $YVO_4:Er^{3+}/Yb^{3+}$ powder, based on upconversion luminescence is sensitive and selective.

7. Spectrum Comparison with Other Er^{3+}/Yb^{3+}-Doped Phosphor Materials

It is clearly observed from Fig. 6 that the red emission intensity is very low, and green emission stands highly prominent. In general, phosphors codoped with Er^{3+} and Yb^{3+} show good

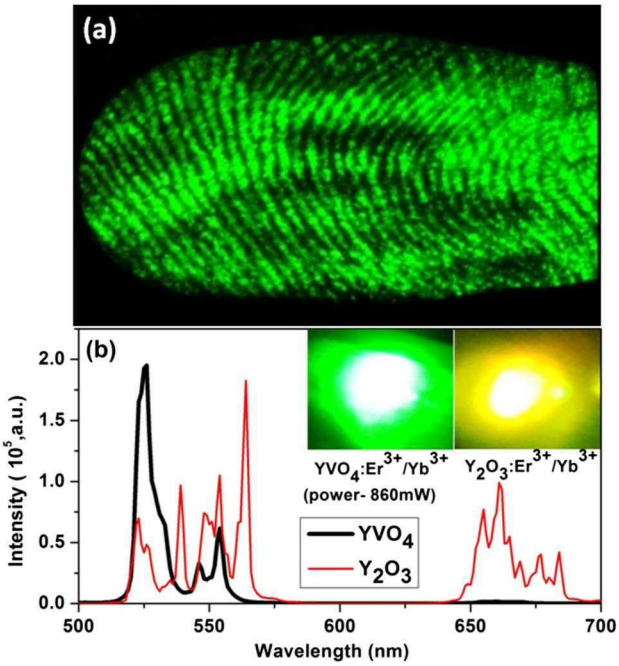

Fig. 10. (a) Fresh fingerprint on glass by dry powdering with $YVO_4:Er^{3+}/Yb^{3+}$, illumination at 980 nm. (b) Comparative spectra of Er^{3+}/Yb^{3+}-codoped YVO_4 and Y_2O_3 phosphors at 860 mW power (inset shows the photographs of the two samples).

Table 1. Variation of Color Coordinates with Power

Power Density (W/cm^2)	Color Coordinates (x, y)
20	0.22, 0.75
55	0.20, 0.76
85	0.19, 0.77
115	0.18, 0.77
150	0.18, 0.77

red emission intensity along with green emission [39,40]. Reduced red emission is a rare case and not observed usually from Er^{3+}/Yb^{3+}-doped samples. A comparison in upconversion emission intensity between Er^{3+}/Yb^{3+}-doped YVO_4 and Y_2O_3 is shown in Fig. 10(b). A clear difference in the emission color is visible in the inset of Fig. 10(b).

Moreover, the color rendering index (CRI) of upconversion emission from the Yb^{3+}/Er^{3+}-codoped YVO_4 nanophosphor is found almost stable against the excitation power. The CRI is calculated at various excitation densities from 20 to 150 W/cm^2, which are tabulated in Table 1.

4. POSSIBLE APPLICATIONS OF THIS MATERIAL

Upconversion phosphors have multidimensional applications. A single-band red upconversion emission was achieved from Er^{3+}/Yb^{3+}-codoped $KMnF_3$ phosphor [41], which is useful for deep tissue imaging. But the use of a green laser is more beneficial than a red laser. Timimi *et al.* [42] has investigated the *in vitro* effect of green light on the rheological properties of human blood and observed that it is not only beneficial for revitalizing the functional capability of preserved blood but also increases the number of blood cells; hence it enhances the function of this blood when injected into a body. In this context, the green emission from our present sample can be used in photodynamic therapy, and we expect the same type of enhanced result as obtained in [39].

Our results have shown that the fluorescence emission intensity ratio of the $^2H_{11/2} \rightarrow {}^4I_{15/2}$ (525 nm) and $^4S_{3/2} \rightarrow {}^4I_{15/2}$ (554 nm) transitions can be employed to measure the temperature of a system noninvasively using the FIR technique with remarkably high sensitivity.

Upconversion phosphors also have shown potential for the conversion of solar energy into electrical energy. Current solar devices are unable to convert the UV and infrared part of the solar spectrum into electrical energy. The absorption of UV causes the creation of hot charge carriers, which dissipate the excess energy by thermalization. So the UV photons are not used efficiently in the solar cells. On the other hand, transmission occurs for photons whose energy is below the bandgap of the semiconductor material resulting in nonabsorption of low-energy photons. Our present material can convert both the infrared as well as ultraviolet radiation into the visible green region. In this regard, Er^{3+}/Yb^{3+}-doped YVO_4 nanophosphor can be used effectively as a spectral converter for solar cells.

Fingerprint detection using the synthesized dry powder of $YVO_4:Er^{3+}/Yb^{3+}$ is effective for latent fingerprint development. The developed images can be visualized as bright green and can be used to detect fingerprints on various surfaces with high contrast without applying specialized equipment.

Other applications are also possible such as making infrared to visible upconverting devices and display systems where pure green light is required. As human sensitivity is highest in the green region, the present phosphor material seems fit for it.

5. CONCLUSIONS

The $YVO_4:Er^{3+}/Yb^{3+}$ microdisk-shaped phosphor is prepared via an easy wet-chemical route. Green emission from the sample is observed on 316 nm excitation due to the efficient energy transfer from host to Er^{3+} ion. Upon 980 nm excitation, the sample showed bright green upconversion with negligible red emission. The fluorescence intensity ratio of two green emission bands ($^4S_{3/2}$ and $^2H_{11/2}$) at different external temperature showed well-fashioned behavior. The synthesized material, $YVO_4:Er^{3+}/Yb^{3+}$, can be used as a cutting-edge temperature sensor with excellent sensitivity using the principle of fluorescence intensity ratio. Observed single green emission is useful in bio-labeling studies for deep tissue imaging. Dry powders of $YVO_4:Er^{3+}/Yb^{3+}$ can be employed for the development of latent fingerprints with high contrast. This material is also favorable to be used as a promising candidate in solar cell concentrators to minimize spectral mismatch.

ACKNOWLEDGMENTS

M. K. Mahata is thankful to the Indian School of Mines, Dhanbad, India, for providing a research fellowship. Dr. K. Kumar is thankful to the Department of Science and Technology (DST) (No. SR/FTP/PS-156/2012), New Delhi, for the financial support.

REFERENCES

1. O. S. Wolfbeis, A. Durkop, M. Wu, and Z. Lin, "A Europium-ion-based luminescent sensing probe for hydrogen peroxide," Angew. Chem., Int. Ed. **41**, 4495–4498 (2002).
2. F. Vetrone, R. Naccache, A. Zamarron, A. Juarranz de la Fuente, F. Sanz-Rodríguez, L. M. Maestro, E. M. Rodríguez, D. Jaque, J. G. Solé, and J. A. Capobianco, "Temperature sensing using fluorescent nanothermometers," ACS Nano **4**, 3254–3258 (2010).
3. T. Justel, H. Nikol, and C. Ronda, "New developments in the field of luminescent materials for lighting and displays," Angew. Chem., Int. Ed. Engl. **37**, 3084–3103 (1998).
4. E. Downing, L. Hesselink, J. Ralston, and R. Macfarlane, "A three-color, solid-state, three-dimensional display," Science **273**, 1185–1189 (1996).
5. A. K. Singh, S. Singh, D. Kumar, D. K. Rai, S. B. Rai, and K. Kumar, "Light-into-heat conversion in $La_2O_3:Er^{3+}$-Yb^{3+} phosphor: an incandescent emission," Opt. Lett. **37**, 776–778 (2012).
6. S. K. Singh, K. Kumar, and S. B. Rai, "Multifunctional Er^{3+}–Yb^{3+} codoped Gd_2O_3 nanocrystalline phosphor synthesized through optimized combustion route," Appl. Phys. B **94**, 165–173 (2009).
7. D. K. Chatterjee and Y. Zhang, "Upconverting nanoparticles as nanotransducers for photodynamic therapy in cancer cells," Nanomedicine **3**, 73–82 (2008).
8. N. M. Idris, Z. Q. Li, L. Ye, E. K. Sim, R. Mahendran, and P. C. Ho, "Tracking transplanted cells in live animal using upconversion fluorescent nanoparticles," Biomaterials **30**, 5104–5113 (2009).
9. N. Kotov, "Bioimaging: the only way is up," Nat. Mater. **10**, 903–904 (2011).
10. S. Sudhagar, S. Sathya, K. Pandian, and B. Lakshmi, "Targeting and sensing cancer cells with ZnO nanoprobes *in vitro*," Biotechnol. Lett. **33**, 1891–1896 (2011).
11. Z. Xu, X. Kang, C. Li, Z. Hou, C. Zhang, D. Yang, G. Li, and J. Lin, "Ln^{3+} (Ln = Eu, Dy, Sm, and Er) ion-doped YVO_4 nano/microcrystals with multiform morphologies: hydrothermal synthesis, growing mechanism, and luminescent properties," Inorg. Chem. **49**, 6706–6715 (2010).

12. W. Ryba-Romanowski, "YVO_4 crystals-puzzles and challenges," Cryst. Res. Technol. **38**, 225–236 (2003).
13. S. A. Miller, H. H. Caspers, and H. E. Rast, "Lattice vibrations of yttrium vanadate," Phys. Rev. **168**, 964–969 (1968).
14. X. Wang, I. Loa, K. Syassen, M. Hanfland, and B. Ferrand, "Structural properties of zircon- and scheelite-type phases of YVO_4 at high pressure," Phys. Rev. B **70**, 064109 (2004).
15. Y. F. Ruan, X. M. Wang, and T. Tsuboi, "Up-conversion in Er^{3+}-doped $LiNbO_3$ crystals," J. Alloys Compd. **275-277**, 246–249 (1998).
16. P. Huang, D. Chen, and Y. Wang, "Host-sensitized multicolor tunable luminescence of lanthanide ion doped one-dimensional YVO_4 nano-crystals," J. Alloys Compd. **509**, 3375–3381 (2011).
17. G. Lakshminarayana, J. Qiu, M. G. Brik, G. A. Kumar, and I. V. Kityk, "Spectral analysis of Er^{3+}-, Er^{3+}/Yb^{3+}- and $Er^{3+}/Tm^{3+}/Yb^{3+}$-doped TeO_2-ZnO-WO_3-TiO_2-Na_2O glasses," J. Phys. Condens. Matter **20**, 375101 (2008).
18. S. Hirano, T. Yogo, K. Kikuta, W. Sakamoto, and H. Koganei, "Synthesis of Nd: YVO_4 thin films by a sol-gel method," J. Am. Ceram. Soc. **79**, 3041–3044 (1996).
19. Y. C. Chen, Y. C. Wu, D. Y. Wang, and T. M. Chen, "Controlled synthesis and luminescent properties of monodispersed PEI-modified YVO_4:Bi^{3+}, Eu^{3+} nanocrystals by a facile hydrothermal process," J. Mater. Chem. **22**, 7961–7969 (2012).
20. K. Riwotzki and M. Haase, "Wet-chemical synthesis of doped colloidal nanoparticles: YVO_4:Ln (Ln = Eu, Sm, Dy)," J. Phys. Chem. B **102**, 10129–10135 (1998).
21. H. Zhang, X. Fu, S. Niu, and Q. Xin, "Synthesis and luminescent properties of nanosized YVO_4:Ln (Ln = Sm, Dy)," J. Alloys Compd. **457**, 61–65 (2008).
22. G. Jia, Y. Song, M. Yang, Y. Huang, L. Zhang, and H. You, "Uniform YVO_4:Ln^{3+} (Ln = Eu, Dy, and Sm) nanocrystals: solvothermal synthesis and luminescence properties," Opt. Mater. (Amsterdam) **31**, 1032–1037 (2009).
23. J. Sun, J. Zhu, X. Liu, and H. Du, "Bright white up-conversion emission from $Er^{3+}/Ho^{3+}/Tm^{3+}/Yb^{3+}$ co-doped YVO_4 phosphors," Mater. Res. Bull. **48**, 2175–2179 (2013).
24. F. S. Ermeneux, R. Moncorge, P. Kabro, J. A. Capobianco, M. Bettinelli, and E. Cavalli, "Crystal growth and luminescence properties of Er^{3+} doped YVO_4 single crystals," in *Advanced Solid State Lasers*, S. Payne and C. Pollack, eds., Vol. **1** of OSA Trends in Optics and Photonics Series(Optical Society of America, 1996), paper SM9.
25. J. A. Coppabianco, P. Kabro, F. S. Ermeneux, R. Moncorge, M. Bettinelli, and E. Cavalli, "Optical spectroscopy, fluorescence dynamics and crystal-field analysis of Er^{3+} in YVO_4," Chem. Phys. **214**, 329–340 (1997).
26. J. Lee and N. A. Kotov, "Thermometer design at the nanoscale," Nano Today **2**(1), 48–51 (2007).
27. S. Som and S. K. Sharma, "Eu^{3+}/Tb^{3+}-codoped Y_2O_3 nanophosphors: Rietveld refinement, bandgap and photoluminescence optimization," J. Phys. D **45**, 415102 (2012).
28. Y. Sun, H. Liu, X. Wang, X. Kon, and H. Zhang, "Combustion synthesis and characterization of Er^{3+} -doped and Er^{3+}, Yb^{3+} -codoped YVO_4 nanophosphors oriented for luminescent biolabeling applications," Chem. Mater. **18**, 2726–2732 (2006).
29. A. E. Morales, E. S. Mora, and U. Pal, "Use of diffuse reflectance spectroscopy for optical characterization of un-supported nanostructures," Rev. Mex. Fis. S **53**, 18–22 (2007).
30. V. Panchal, D. Errandonea, A. Segura, P. Rodríguez-Hernandez, A. Muñoz, S. Lopez-Moreno, and M. Bettinelli, "The electronic structure of zircon-type orthovanadates: effects of high-pressure and cation substitution," J. Appl. Phys. **110**, 043723 (2011).
31. M. K. Mahata, K. Kumar, and V. K. Rai, "Structural and optical properties of Er^{3+}/Yb^{3+} doped barium titanate phosphor prepared by co-precipitation method," Spectrochim. Acta, Part A **124**, 285–291 (2014).
32. J. F. Suyver, A. Aebischer, S. García-Revilla, P. Gerner, and H. U. Güdel, "Anomalous power dependence of sensitized upconversion luminescence," Phys. Rev. B **71**, 125123 (2005).
33. H. Guo, N. Dong, M. Yin, W. Zhang, L. Lou, and S. Xia, "Visible upconversion in rare earth ion-doped Gd_2O_3 nanocrystals," J. Phys. Chem. B **108**, 19205–19209 (2004).
34. M. P. Hehlen, N. J. Cockroft, and T. R. Gosnell, "Spectroscopic properties of Er^{3+} and Yb^{3+} doped soda-lime silicate and aluminosilicate glasses," Phys. Rev. B **56**, 9302–9318 (1997).
35. S. A. Wade, S. F. Collins, and G. W. Baxter, "Fluorescence intensity ratio technique for optical fiber point temperature sensing," J. Appl. Phys. **94**, 4743–4756 (2003).
36. M. K. Mahata, A. Kumari, V. K. Rai, and K. Kumar, "Er^{3+}, Yb^{3+} doped yttrium oxide phosphor as a temperature sensor," AIP Conf. Proc. **1536**, 1270–1271 (2013).
37. M. Quintanilla, E. Cantelar, F. Cusso, M. Villegas, and A. C. Caballero, "Temperature sensing with up-converting submicron-sized $LiNbO_3$:Er^{3+}/Yb^{3+} particles," Appl. Phys. Express **4**, 022601 (2011).
38. C. Champod, C. Lennard, P. Margot, and M. Stoilovic, *Fingerprint and Other Ridge Skin Impression* (CRC Press, 2004).
39. V. Singh, V. K. Rai, and M. Haase, "Intense green and red upconversion emission of Er^{3+}, Yb^{3+} co-doped $CaZrO_3$ obtained by a solution combustion reaction," J. Appl. Phys. **112**, 063105 (2012).
40. D. Gao, X. Zhang, and W. Gao, "Tuning upconversion emission by controlling particle shape in $NaYF_4$:Yb^{3+}/Er^{3+} nanocrystals," J. Appl. Phys. **111**, 033505 (2012).
41. J. Wang, F. Wang, C. Wang, Z. Liu, and X. Liu, "Single-band upconversion emission in lanthanide-doped $KMnF_3$ nanocrystals," Angew. Chem., Int. Ed. **50**, 10369–10372 (2011).
42. Z. A. Timimi, M. S. Jaafar, and M. Z. M. Jafri, "Photodynamic therapy and green laser blood therapy," Glob. J. Med. Res. **11**, 22–27 (2011).